Ultrafast diffraction conoscopy of the structural phase transition in VO_2: Evidence of two lattice distortions

Nardeep Kumar, Armando Rúa, Félix E. Fernández, and Sergiy Lysenko*
Department of Physics, University of Puerto Rico, Mayaguez, Puerto Rico 00681, USA
(Received 21 March 2017; revised manuscript received 22 May 2017; published 30 June 2017)

Photoinduced phase transitions in complex correlated systems occur very rapidly and involve the interplay between various electronic and lattice degrees of freedom. For these materials to be considered for practical applications, it is important to discover how their phase transitions take place. Here we use a novel ultrafast diffraction conoscopy technique to study the evolution of vanadium dioxide (VO_2) from biaxial to uniaxial symmetry. A key finding in this study is an additional relaxation process through which the phase transition takes place. Our results show that the biaxial monoclinic crystal initially, within the first 100–300 fs, transforms to a transient biaxial crystal, and within the next 300–400 fs converts into a uniaxial rutile crystal. The characteristic times for these transitions depend on film morphology and are presumably altered by misfit strain. We take advantage of Landau phenomenology to describe the complex dynamics of VO_2 phase transition in the femtosecond regime.

DOI: 10.1103/PhysRevB.95.235157

I. INTRODUCTION

Discovery of a phase transition near room temperature of ∼340 K, accompanied by a dramatic insulator-to-metal change in electrical properties [1], made VO_2 one of the highly investigated strongly correlated electronic materials. The VO_2 complex phase transition involves electron-electron correlations and electron-lattice interactions [2,3], which makes it challenging to determine the transition processes [4–6]. Along with temperature [1], the VO_2 phase transition can also be triggered by a number of different external excitations such as pressure [7], strain [8], doping [9], or light [10]. Out of these external excitations, light with ultrashort laser pulses allows monitoring the phase-transition dynamics on an ultrafast timescale [11]. In the past decades, several enthralling results on VO_2, obtained by using optical [11–17], terahertz [18–21], x-ray [10,22–27], and electron diffraction [28–30], methods increased our understanding regarding its phase transition.

VO_2 is one of the intensively studied transition-metal oxides and a large number of studies have been devoted to the finding of driving mechanisms behind its phase transition. There is a long standing debate over the two mechanisms, Mott or Peierls type, believed to be responsible for the VO_2 phase transition [12,31–35]. Within this long standing debate, much less attention has been paid to the structural phase transition (SPT) dynamics on a femtosecond timescale. An important study related to the VO_2 phase-transition process involves determining the stages through which a monoclinic biaxial crystal transforms to a rutile uniaxial crystal. One way to study SPT dynamics in the femtosecond regime is by tracking only the structural degrees of freedom. Conventional optical pump-probe methods provide a collective response of lattice and electron dynamics. To separate the lattice relaxation component from the pure electronic response in a transient nonlinear optical signal is a nontrivial task and new experimental approaches are required.

In this paper, we present a method of ultrafast diffraction conoscopy (UDC) which allows us to track the transient change of lattice symmetry. By monitoring the transient polarization of scattered light along with the evolution of conoscopy patterns, the UDC reveals two different components of VO_2 lattice distortion on a subpicosecond timescale. The structural phase transition occurs from a monoclinic biaxial to rutile uniaxial crystal and follows a complex phase trajectory via a transient intermediate state with biaxial symmetry. Observed nonequilibrium structural dynamics is supported by a quantitative analysis in terms of the Ginzburg–Landau formalism.

II. EXPERIMENT

A. Sample preparation and characterization

Thin films of VO_2 with various thicknesses were grown on single-crystal (110) Al_2O_3 (A cut) and (100) Al_2O_3 (M cut) substrates by using a pulsed laser deposition technique. For these samples, the laser ablation process was performed by using an excimer laser (KrF, 248 nm wavelength) with 25 ns pulses. The process was carried out at 4 J/cm^2 fluence with a chamber pressure of 50 mTorr, argon and oxygen gas flows of 10 and 15 standard cubic centimeters per minute, respectively, and substrate temperatures of 550 °C. The x-ray diffraction (XRD) patterns of all VO_2 films provide evidence of the single monoclinic M_1 phase at room temperature, with good off-plane and in-plane orientation with respect to the sapphire substrates which can be described as epitaxial. Atomic force microscopy (AFM) and XRD analyses were performed to verify the quality and orientation of the films, as shown in supplementary Figs. 2 and 3, respectively [36].

B. Ultrafast diffraction conoscopy

The experiment to study light-induced SPT dynamics of VO_2 was performed with a scatterometer setup schematically shown in Fig. 1. A titanium sapphire laser (Ti:sapphire) provides ultrashort pulses with a central wavelength of $\lambda =$ 800 nm and a repetition rate of 80 MHz. The output from the

*sergiy.lysenko@upr.edu

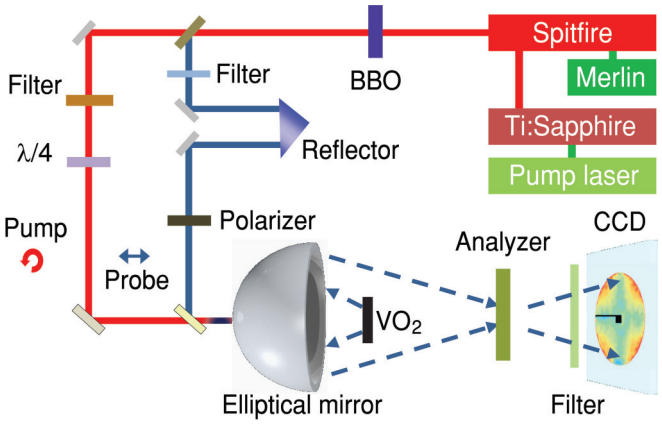

FIG. 1. Schematics of the experimental setup for polarization-resolved light scattering measurements.

Ti:sapphire laser is sent to a regenerative amplifier (Spectra–Physics Spitfire) which is pumped by a Nd:YLF laser (Merlin) of 8 W average output and a repetition rate of 1 kHz. The regenerative optical amplifier provides 800 nm wavelength output with pulse time duration between 80 and 130 fs and 1 kHz repetition rate, which is used as a pump beam. The second-harmonic pulse, which acts as a probe, with a central wavelength of 400 nm, is obtained by using a beta barium borate (BBO) nonlinear crystal.

The phase transition was triggered by the circularly polarized pump pulse focused to a spot size of 0.6 mm. Circular polarization was used to avoid possible artifacts owing to the photoinduced anisotropy of VO_2 electronic density that is not actually related to lattice symmetry. To monitor the phase transition, the vertically polarized probe pulse was focused into a tighter spot of 70 μm diameter. Both pump and probe pulses were incident normal to the sample surface, which was mounted on a rotational holder. The time delay between pump and probe pulses was controlled by using a retroreflector in the probe arm. Scattered light from the sample was collected by an elliptical mirror which focused the light to a charge-coupled device (CCD). The pump beam was prevented from reaching the detector by using a color filter.

The scattering distribution signal was measured and mapped as a bidirectional-scatter distribution function (BSDF) versus polar angle θ and azimuthal angle φ. The BSDF is defined as follows [37]:

$$\mathrm{BSDF}(\theta,\varphi) = \frac{1}{I_0}\left(\frac{dI_{\mathrm{scatt}}(\theta,\varphi)}{d\Omega}\right)\frac{1}{\cos\theta}, \qquad (1)$$

where I_0 is the intensity of incident light, and dI_{scatt} is the intensity of light scattered into solid angle $d\Omega$. To record the conoscopy images an analyzer is inserted between the CCD and elliptical mirror at horizontal polarization. The transient scattering signal is maximal when the VO_2 optical axis is tilted at a specific angle with respect to the probe polarization so that there is a stronger change of elliptical polarization of scattered light during the SPT. Therefore, samples were rotated to a position of highest transient modulation of scattering signal. The measurements were performed at room temperature.

The conoscopy technique is based on angle-resolved elastic light scattering and employs two crossed linear polarizers before and after the elliptical mirror (Fig. 1). Light scattering is a process directly related to surface irregularities and optical properties and provides information about material inhomogeneities [38–41]. The UDC technique is useful for statistical analysis of transient crystallographic symmetry of polydomain highly orientated films with a thickness about one order of magnitude less than the laser probe wavelength. This method is based on the fact that the crystal anisotropy produces optical birefringence and splits linearly polarized light into two mutually orthogonal components with different phase velocities. Due to cumulative phase difference of these components, the scattered light becomes elliptically polarized. The degree of elliptical polarization and the shape of conoscopy pattern were monitored by using a CCD detector equipped by a linear polarizer (analyzer).

UDC allows us to separate signals related only to the lattice symmetry transformation from other types of signals (band filling, change of optical constants during phase transition, etc.), which is an important advantage of this technique. A noticeable contribution in light depolarization arises from Rayleigh scattering which allows us to monitor birefringence of microcrystals with sizes much less than the light wavelength.

III. RESULTS

Figure 2(a) shows the bidirectional scatter distribution function (BSDF) indicatrices of hemispherical light scattering from a 40-nm-thick VO_2 film on a sapphire substrate (A cut) as a function of both polar and azimuthal angles. The distinctive conoscopy patterns at different probe delays are outlined by dashed isophotes. For these scans, the energy fluence of the pump pulses was 14 mJ/cm^2. In the first few hundred femtoseconds, the scattering signal consists of two hyperbolas, similar to biaxial isogyres [see Fig. 3(d) in the Supplemental Material [36]], in opposite quadrants, which transform to a cross-like pattern, similar to uniaxial isogyres [see Fig. 3(b) in the Supplemental Material [36]], at the end of the phase transition. Figure 2(c) represents the cross sections of the scattering indicatrix for probe delays of 25, 330, 540, and 800 fs, along an azimuthal angle $\varphi = 225^\circ$. The most obvious nontrivial observation from these BSDF curves is that the intensity minimum shifts significantly during the SPT interval. This noticeable shift reflects the change in the conoscopy pattern as a result of lattice transformation.

To investigate the evolution of the VO_2 system through SPT, we take polar angles corresponding to BSDF minimum of scattering indicatrix curves at various probe delays and plot, as shown in Fig. 2(d), for different pump fluences. From this BSDF minimum shift trend, two distinct processes can be resolved: (1) during the first ~300 fs the initial monoclinic lattice of VO_2 transforms into a nonequilibrium biaxial phase which appears as an increase of the angular position of the BSDF minimum and (2) after ~300 fs the angular position of the BSDF minimum starts to decrease, attaining a constant value within 500–700 fs. In discussing this transition, we define some characteristic times in Fig. 2(d), where the time T1 represents zero delay, the time T2 is defined by the extreme of minimum change, and T3 is where the shift reaches a steady level. Tji is defined as the time difference between times i and j. The shift reaches a peak at T2 within 300 fs after zero

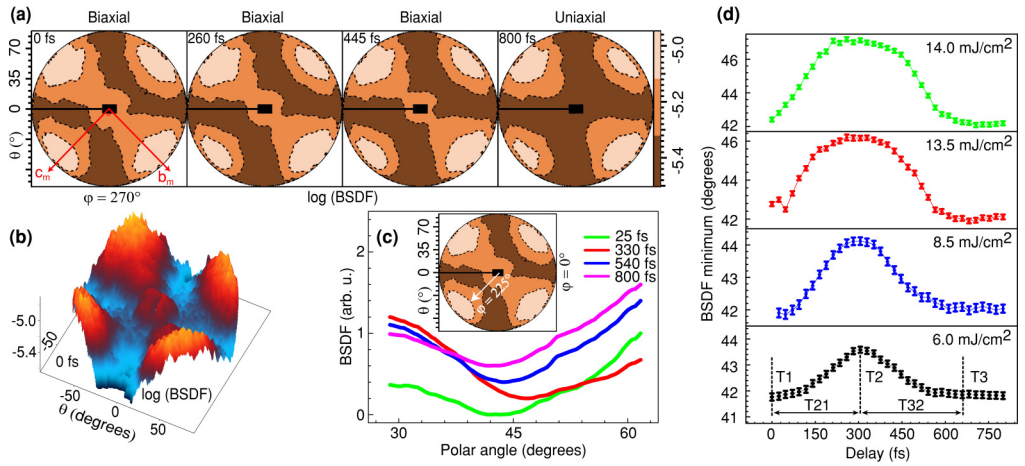

FIG. 2. Ultrafast diffraction conoscopy of VO_2 film on A-cut Al_2O_3. (a) Evolution of the light scattering indicatrix showing the transformation of biaxial isogyres to uniaxial isogyres. The distinctive conoscopy patterns are outlined by dashed isophotes. The black rectangular region along with a black bar shows the location of the sample holder. (b) Three-dimensional view of light scattering indicatrix showing conoscopy patterns at 0 fs. (c) Cross sections of the scattering indicatrix along an azimuthal angle $\varphi = 225^\circ$ for 25, 330, 540, and 800 fs. The arrow in the inset shows the azimuthal direction of the cross sections. (d) Temporal position of BSDF minimum of scattering indicatrix cross section at $\varphi = 225^\circ$ for various pump fluences. Error bars represent the standard deviation obtained from multiple measurements to collect BSDF minimum shift.

delay. After a period of $\Delta T21 = 300$ fs, the shift starts to decrease for a period of $\Delta T32 = 300$–400 fs and reaches a minimum at T3. After that, the shift reaches a steady level, which corresponds to the end of the subpicosecond phase transition.

The light scattering intensity is proportional to the squared value of optical polarizability and surface roughness [37,43]. The absolute value of the VO_2 dielectric constant and, as a consequence, its polarizability, is lower for the metallic phase [44]. As shown in Refs. [45,46], the surface geometry does not change during the ultrafast phase transition, and the light scattering intensity decreases due to the transient change of VO_2 optical properties. Hence, if the phase transition is a single-stage process, then the BSDF minimum should shift monotonically. However, the fact that it first increases and then decreases indicates that the initial monoclinic lattice transforms to a different biaxial crystal. Although the actual crystal symmetry of this transient phase is unknown, it is definitely a biaxial crystal, as evidenced in the indicatrix sequence in Fig. 2(a). Furthermore, the increase of pump fluence results in a larger transient change of this angular position due to a higher level of photoinduced metastability accompanied by stronger lattice distortion.

To further investigate the rich dynamics of the VO_2 phase transition and also to support results of Fig. 2(d), we map the UDC data as a relative change of measured signal $\Delta BSDF(t)/BSDF(0)$, where $\Delta BSDF(t) = BSDF(t) - BSDF(0)$ as shown in Fig. 3(a). These data represent the evolution of polarization state of light scattering from VO_2 film. Here an emerging rectangular region with larger positive $\Delta BSDF(t)/BSDF(0)$ values, peaks at 250–350 fs and then starts to decrease and disappears after 500–700 fs (see movie 1 in the Supplemental Material [42]). This behavior can be ascribed to a two-stage phase transition which causes an increase followed by a decrease in differential scattering. It is noted that the time for the maximum differential scattering signal coincides with the characteristic time T2 for BSDF minimum [see Fig. 2(d)].

To trace the change of light polarization due to lattice transformation into an intermediate transient state, we define an arbitrary parameter Wr as the width of the rectangular region at an azimuthal angle of $\varphi = 225^\circ$. The measured width (Wr) in angular units for various time delays is shown in Fig. 3(b). Due to the low resolution near zero delay, we measured Wr starting from 100 fs. The change of the width with time delay follows the same trend as seen from the position of the BSDF minimum in Fig. 2(d). From these results, we conclude that the observed phase transition is dominated by biaxial symmetry, which changes to uniaxial within the 500–700 fs time interval. Our results for the shift of BSDF minimum and relative change of differential scattering provide solid evidence for the existence of a two-stage phase transition in VO_2. Next, we explore the phase-transition trend by using total integrated scattering over a hemisphere without analyzer and compare the results with those for UDC patterns. Figure 3(c) shows the total integrated scattering signal I_S/I_0 as a function of the probe delay for the first 800 fs. From this curve, we deduced the phase-transition characteristic time on the order of 400 fs.

The complex dynamics of photoinduced phase transition results in a gradual change of the VO_2 band structure on the femtosecond timescale. Ordinary pump-probe optical techniques which utilize transient transmission, reflection, or total integrated scatter show a monotonic step-like change of the optical signal as VO_2 switches to its final rutile phase. However, these techniques only partially resolve lattice relaxation dynamics, and many features remain hidden. After a rigorous analysis of experimental data, several works [16,28,29,46,47] reported the presence of at least two stages of phase transition. Here, by applying the UDC technique, the two stages of the SPT process can be clearly resolved on a femtosecond timescale, as shown in Fig. 3(d). As expected, when VO_2 completely switches into a final rutile phase within 700 fs,

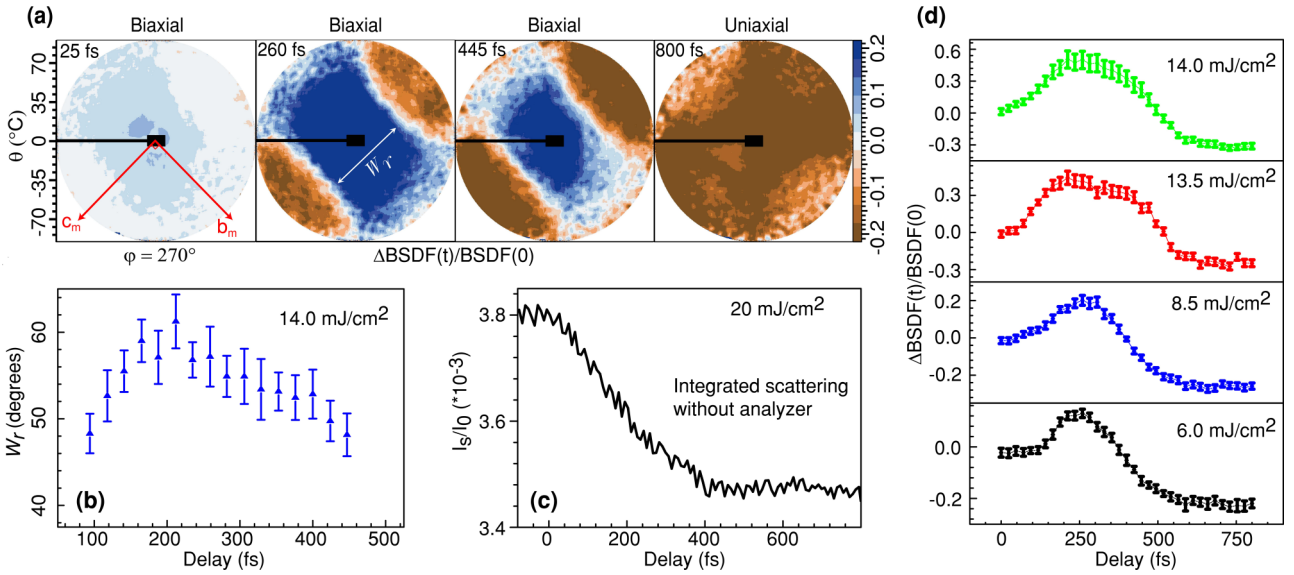

FIG. 3. Evolution of polarization state of light scattering from VO_2 film on A-cut Al_2O_3. (a) Relative change of UDC indicatrix $\Delta\text{BSDF(t)}/R_{\text{BSDF}}(0)$. A rectangular region, ascribed to a multistage phase transition, emerging at the beginning of the phase transition reaches a peak between 250–350 fs and then starts to decrease and disappears after 500–700 fs (see movie 1 in the Supplemental Material [42]). (b) Change of the width (Wr) of the dark rectangular region at an azimuthal angle of $\varphi = 225^\circ$ with respect to the probe delay. Width was measured from 95 to 470 fs due to the low resolution outside this interval. (c) Light scattering, integrated over the hemisphere without analyzer, as a function of probe delay for a pump fluence of 20 mJ/cm^2. (d) UDC: cross-section of ΔBSDF(t)/BSDF(0) at $\varphi = 225^\circ$ for various pump fluences. Error bars represent the standard deviation obtained from multiple measurements.

the total change of the scattering signal is nearly independent of pump fluence. However, at ~300 fs, increasing excitation level results in the significant rise of the ΔBSDF(t)/BSDF(0) UDC signal. This behavior is associated with a higher level of photoinduced metastability, which provides stronger transient lattice distortion and, as a consequence, higher depolarization of scattered light.

To demonstrate the influence of crystal orientation on the transient UDC indicatrix, we rotated the sample by -45° from the original orientation in Figs. 2 and 3. The resulting differential UDC patterns are shown in Fig. 4(a). At this orientation of the sample, the b_m axis of VO_2 lattice coincides with the polarization plane of the probe beam. As a result,

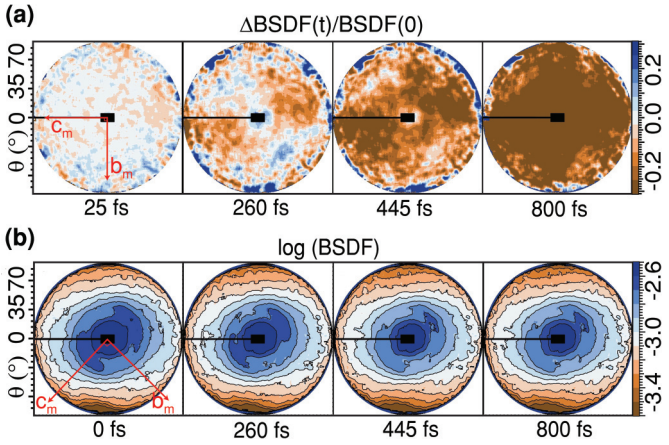

FIG. 4. Transient light scattering from VO_2 films on A-cut Al_2O_3. (a) Relative change ΔBSDF(t)/BSDF(0) of UDC indicatrix. The sample is rotated by -45° from the original orientation in Figs. 2 and 3. (b) Evolution of light scattering indicatrix without an analyzer.

the ΔBSDF(t)/BSDF(0) signal drops monotonically, without showing noticeable light depolarization.

To compare UDC results with ultrafast light scattering, we collected scattering data by removing the analyzer from the setup. The BSDF indicatrices, measured as a function of both θ and φ, with respect to probe delay, are shown in Fig. 4(b). As expected, the scattering indicatrices show only a continuous decrease of the signal without any noticeable intermediate transition, same as seen for total integrated scattering [Fig. 3(c)]. An elliptical-type pattern can be observed in these indicatrices due to the multidomain epitaxial nature of the film, which means that there are strongly preferential lateral orientations of the VO_2 lattice with respect to the substrate. These results highlight the relevance of the UDC for studies of the transformation.

To explore the effects of thickness and misfit strain, we also investigated thicker VO_2 (80 nm) samples grown on A-cut (110 plane) and M-cut (100 plane) sapphire substrates. The azimuthal orientation of the samples was set to obtain maximal differential, ΔBSDF(t)/BSDF(0), signal. Time-resolved diffraction conoscopy indicatrices from VO_2 films on A-cut and M-cut substrates are shown in Figs. 5 and 6, respectively. The scattering data for all the samples are compared with respect to their orientation along the probe direction. By comparing 40 and 80 nm VO_2 samples on A-cut substrates, the conoscopy patterns in the case of the thicker film are less sharp. However, the change from biaxial to uniaxial symmetry is still visible (Fig. 5). Similarly, for the 80-nm-thick VO_2 film on M-cut sapphire the change in conoscopy patterns clearly indicates biaxial to uniaxial transformation. Differential scattering [Fig. 6(b)] shows a sharp square-like feature due to the preferable orientation of VO_2 grains and domains on a single-crystal Al_2O_3 substrate, as confirmed by

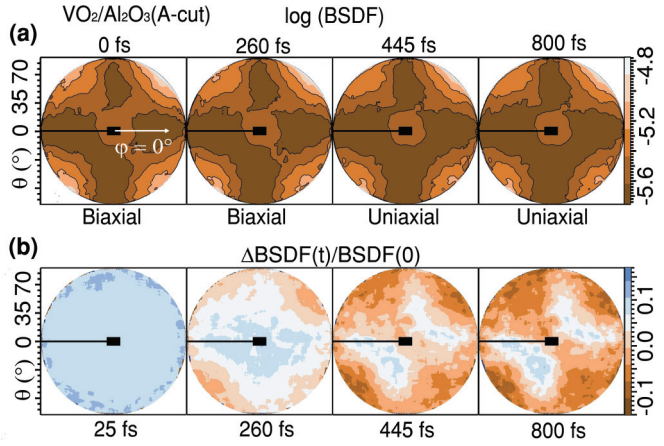

FIG. 5. The light scattering from 80-nm-thick VO_2 film on A-cut Al_2O_3. (a) Evolution of UDC indicatrix during the transformation of VO_2 from biaxial to the uniaxial crystal at 14.0 mJ/cm^2 excitation. (b) Relative change of transient conoscopy signal ΔBSDF(t)/BSDF(0).

x-ray measurements versus azimuthal orientation of the sample [see Figs. 2(c) and 2(d) in the Supplemental Material [36]).

Figure 7 shows the cross sections of UDC patterns along the azimuthal directions with stronger light depolarization for all the three samples. As can be clearly seen in the case of the 40-nm-thick VO_2 film on A-cut sapphire, the first stage in the transition process reaches an extreme, shown by a vertical dashed line, in about 250–300 fs, and is then followed by a second stage which decays within the next 300–400 fs. However, in the case of thicker samples on A- and M-cut sapphire substrates the first stage occurs twice as fast than for the thin sample. This implies that the intermediate biaxial state lasts longer in thinner films, which are expected to have higher strain, as compared with thicker films.

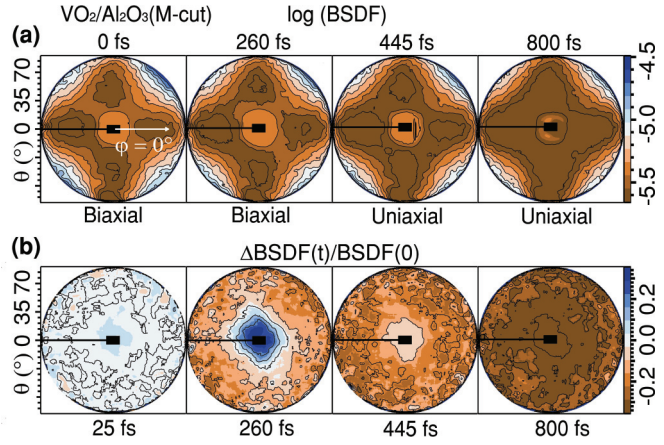

FIG. 6. The light scattering from 80-nm-thick VO_2 films on M-cut Al_2O_3. (a) Evolution of UDC indicatrix during transformation of VO_2 from biaxial to the uniaxial crystal at 14.0 mJ/cm^2 laser excitation. (b) Transient change of relative conoscopy signal ΔBSDF(t)/BSDF(0).

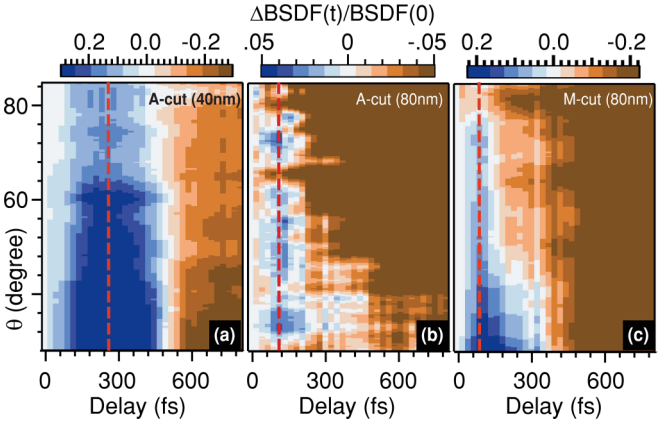

FIG. 7. Cross sections of UDC patterns from three VO_2 samples for different polar angles at azimuthal angle $\varphi = 285^\circ$ with respect to time delay. ΔBSDF(t)/BSDF(0) distribution for (a) 40 nm VO_2 film on A-cut Al_2O_3, (b) 80 nm VO_2 films on A-cut Al_2O_3, (c) 80 nm VO_2 films on M-cut Al_2O_3. Cross-section maps clearly show the difference between phase-transition dynamics in three VO_2 samples. In the case of a 40 nm sample on A-cut sapphire, the first stage in the transition process reaches an extreme in about 300 fs and is then followed by a second stage which decays within 300–400 fs. The first stage is twice as fast in thicker samples on A- and M-cut sapphire substrates. Vertical dashed lines indicate the maximum of ΔBSDF(t)/BSDF(0) signal related to the intermediate biaxial state.

IV. DISCUSSION

Time-resolved diffraction conoscopy allows monitoring the transformation of lattice symmetry in epitaxial or textured films with thicknesses much smaller than the wavelength of incident light. Moreover, the obtained data are statistically averaged over thousands of microcrystals within the illuminated area. Thus, the UDC technique can provide information about structural relaxation for thin polydomain films, as long as transient light depolarization or a transient conoscopy patterns can be detected. The presence of VO_2 domains with different orientations results in a smearing of the conoscopy patterns; however, this does not affect the pathway of structural transformation. We note that, for all the studied films, we observed very similar transient behavior and a pronounced change of scattering signal and conoscopy patterns.

The biaxial-to-uniaxial ultrafast phase transition in VO_2 takes place in two stages and can be considered as related to two different lattice distortions similar to those discussed by Goodenough [2]. It should be noted here that we have observed two components of the SPT for three VO_2 films with substantially different morphology, and these two components are associated with two different characteristic lattice distortions with different relaxation times. Moreover, for the thinner film, which is expected to have a higher misfit strain, the characteristic relaxation time of the first transition stage is 250–300 fs [Figs. 2, 3, and 7(a)] which is twice as slow as for the thicker films [Figs. 7(b) and 7(c)]. This fact suggests that strain is one of the key parameters controlling ultrafast lattice relaxation dynamics.

While two distinct lattice relaxation processes are observed, the starting point of the second process is difficult to resolve with high accuracy. It is very likely that the light pulse triggers

two lattice relaxation processes simultaneously, but the internal strain in the film alters the relaxation time of each characteristic lattice distortion and affects the total pathway of the SPT which appears as a two-stage process. The first stage of SPT is related to the initial transition to a transient state with biaxial symmetry. This process is mainly associated with the antiferroelectric lattice distortion. The second stage of SPT is related to the lattice transformation into the rutile phase, with uniaxial symmetry, and can be assigned to V-V bonding.

Here we note that the total light-induced SPT in a thin VO_2 film occurs simultaneously in all grains of the film within several hundred femtoseconds. Several studies of transient surface statistics [45,46] have shown the absence of coexistence of different VO_2 phases during the ultrafast phase transition. While slight variation of characteristic transition time was observed versus grain size, the pathway of SPT was identified as a coherent process across all spatial frequencies of the surface. Moreover, on femto- and picosecond timescales only short-range phonon interactions take place [45,46]. As a result, the ultrafast phase transition does not noticeably contribute to formation of new domains within several picoseconds.

The ultrafast first-order phase transition can be analyzed in terms of Ginzburg–Landau theory [48–50]. The experimentally observed SPT dynamics can be supported by modeling of thermodynamic potential Φ for photoexcited VO_2, as shown in Fig. 8. To estimate the profile of thermodynamic potential, we performed calculations of molecular dynamics and measured transient reflection and transmission of VO_2 films (see Supplemental Material [36]). Measurements of relaxation rates on the picosecond timescale allowed us to estimate the profile of Φ. Two different components of VO_2 lattice distortion revealed by UDC can be associated with two effective ion displacements x_1 and x_2, which correspond to antiferroelectric distortion and V-V bonding, respectively. Taking into account only the insulating M_1 and metallic R phase of VO_2, the thermodynamic potential Φ consists of two potential wells separated by a barrier ΔG. The two-well potential model does not explicitly imply the presence of an intermediate state of VO_2, but it can be used for analyses of two different lattice distortions.

The two-well lattice thermodynamic potential Φ can be described by employing the following ansatz [50]:

$$\Phi = \frac{\alpha(F)}{2}\left(x_1^2 + x_2^2\right) + \frac{\beta_1}{4}(2x_1x_2)^2 + \frac{\beta_2}{4}\left(x_1^2 - x_2^2\right)^2 + \frac{\gamma}{6}\left(x_1^2 + x_2^2\right)^3, \quad (2)$$

where F is laser fluence and $\alpha(F)$, β_1, β_1, and γ are experimentally derived constants. These constants were estimated from additional measurements of the slower (picosecond) component of VO_2 relaxation dynamics which was detected after the ultrafast subpicosecond transition at excitation fluence below 30 mJ/cm^2.

We assume that the concentration of photoexcited free carriers is the main factor that alters Φ, and x_1 and x_2 correspond to the whole displacement of VO_2 sublattices during antiferroelectric distortion and V-V bonding, correspondingly. The VO_2 lattice motion is oscillatory in nature, and it has been shown by many groups that it oscillates with a frequency of 6 THz [3,16–18,51,52]. Taking into account the relaxation nature of these oscillations, we obtain the equation of motion [53]:

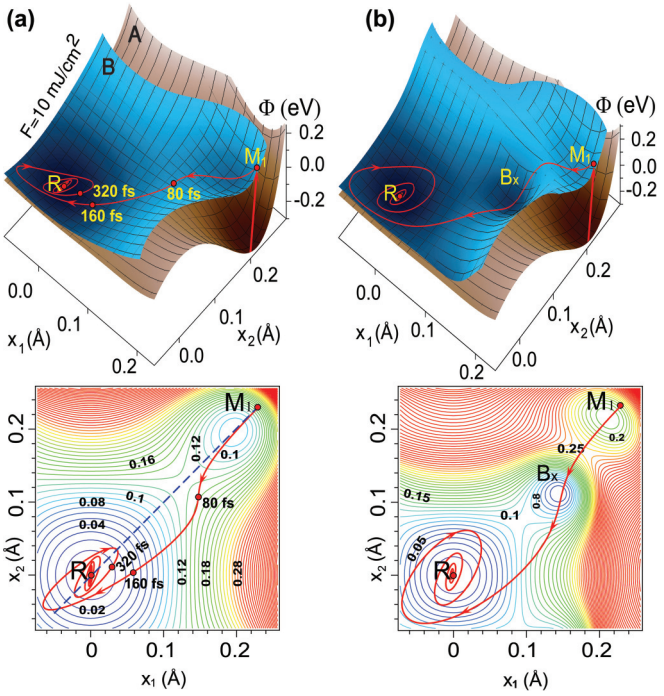

FIG. 8. Phase trajectory of photoexcited VO_2. The solid line with arrows shows the pathway of the energy relaxation after photoinduced change of thermodynamic potential. Two potential-energy surfaces, marked by A and B, correspond to unperturbed and photoexcited states of VO_2 respectively. (a) A double-well potential case. This model implies the presence of only M_1 and R phases. Dashed line indicates the phase trajectory for the case of equal relaxation rates for antiferroelectric distortion (x_1) and V-V bonding (x_2). (b) A triple-well thermodynamic potential. The possible intermediate phase is denoted by B_x.

$$\ddot{x}_i + 2g_i\dot{x}_i = -\frac{1}{\tilde{m}}\frac{\partial\Phi}{\partial x_i}, \quad (3)$$

where $\tilde{m}$ is the effective mass and g_i is the damping coefficient, related to the experimentally measured transition rate for each distortion i of the phase transition. For two observed distortions, damping coefficients $g_1 = 6.7 \times 10^{12}$ s^{-1} and $g_2 = 2.1 \times 10^{12}$ s^{-1} were calculated by using the experimental data of Figs. 2 and 3. By using the thermodynamic potential Φ and frequency 6 THz of the optical phonon mode, the effective mass $\tilde{m}$ was estimated to be 1.7×10^{-25} kg.

Figure 8(a) shows the pathway of the energy relaxation obtained by numerical integration of Eq. (3) for the ultrafast first-order phase transition. Here, the photoexcitation of the free carriers instantaneously modifies the thermodynamic potential Φ by screening the Coulomb repulsion and switching the VO_2 lattice into a nonequilibrium excited state [54,55]. In case of absence of internal strain, our model assumes that the relaxation rates for two distortions x_1 and x_2 are equal. As a result, the phase trajectory of the phase transition is just a simple transition from monoclinic phase to rutile phase denoted by a straight dashed line "M_1-R" on the potential landscape in Fig. 8(a). This transition would result in a monotonic

decrease of light depolarization during the transition. However, experimental observations of lattice dynamics by UDC shows significant transient depolarization of light scattering for all samples due to deviation of the actual phase trajectory from the M_1-R straight line. Since the lifetime of the transient biaxial phase depends on the type and thickness of the epitaxial film (Fig. 7), it is believed that the internal misfit strain increases this deviation via the difference in the relaxation rate for antiferroelectric distortion and V-V bonding.

The UDC data for 40 nm VO_2/Al_2O_3 (A cut) shows a significant rise of the transient depolarization within 300 fs [Figs. 2 and 7(a)], a timescale which is nearly twice as long as the oscillation period of VO_2 optical phonons (see Sec. V in the Supplemental Material [36]). This relatively long time can correspond not only to different relaxation rates for distortions x_1 and x_2, but also to the presence of an intermediate biaxial phase and additional third potential well on the Φ landscape denoted by B_x, as shown in Fig. 8(b). Upon light-induced phase transition, the lattice symmetry changes from monoclinic to rutile via B_x, moving along some complex phase trajectory.

Recently, several studies using temperature [17,56–59], pressure [60–63], light [29,35,47,55], and voltage [27] have demonstrated that the VO_2 phase transition takes place through an intermediate phase with monoclinic symmetry. Bai *et al.* suggest the presence of several new phases (e.g., distorted M_1, orthorhombic, X phase) under high pressure [61]. In the case of photoinduced SPT, the initial excited state corresponds to the M_1 phase, while the transient biaxial phase B_x can be the M_2 or orthorhombic phase. However, the exact symmetry of the B_x phase cannot be determined by the optical UDC technique. Nevertheless, the transient B_x phase is definitely a biaxial phase which is different from initial M_1 and final rutile phase.

The presence of two different lattice distortions in ultrafast phase transition reveals a resemblance between light-induced and thermally induced crystallographic transitions in terms of Goodenough's model, proposed in his seminal work [2]. According to Goodenough, two distinguishable components of lattice distortion are present: antiferroelectric distortion into an orthorhombic structure and homopolar V-V bonding along the a_m axis. For pure and unstrained VO_2 these distortions occur at the same temperature. However, doping or mechanical strain both separate the temperatures at which they occur. In our case, it is very likely that the strain affects the SPT in a similar way, resulting in a structural transition from monoclinic to an intermediate phase before transforming to a rutile symmetry. This concept agrees with Goodenough's prediction about an orthorhombic intermediate phase which is also biaxial in nature. There have been numerous studies demonstrating that strain is one of the key parameters which alters the phase-transition pathway [23,58,64–84]. Laverock *et al.* provide conclusive evidence that the observed intermediate phase is accessible in the ground state at ambient temperatures and pressures in epitaxially strained VO_2 [58].

For a triple-well thermodynamic potential the quantitative theoretical analysis of the SPT dynamics becomes rather difficult. However, qualitative estimation shows that the additional potential well can noticeably increase the transient time of the nonequilibrium biaxial state. The presence of an additional potential well in Φ can significantly increase the difference in the relaxation rate for antiferroelectric distortion and V-V bonding and, as a result, increase the depolarization time of scattered light observed by UDC. During this SPT, the relaxation rate can be a function of time (i.e., damping of vibrational modes can change during SPT). Taking into account the significant differences in relaxation dynamics of epitaxial VO_2 films on different substrates (Fig. 7), it is very likely that the depth of the potential well B_x for transient intermediate phase depends on film morphology and internal strain.

V. CONCLUSION

In conclusion, we have shown that femtosecond pump-probe diffraction conoscopy is a powerful technique to track the structural phase-transition dynamics in complex correlated materials. A pronounced two-stage process in the phase transition of VO_2 was observed with two distinct characteristic times. After the phase transition is triggered by a light pulse, the monoclinic biaxial crystal transforms to a transient biaxial crystal which is the first stage of the phase transition lasting for 100–300 fs. The second stage lasts for the next 300–400 fs and is related to the lattice transformation from transient biaxial phase into the rutile uniaxial phase. It is most likely that the internal misfit strain in epitaxial film alters the observed characteristic relaxation times. By applying Ginzburg–Landau formalism it is shown that the observed two-stage UDC dynamics originates from two lattice distortions with different relaxation times. According to Goodenough's model of VO_2 lattice instability, these distortions can be associated with antiferroelectric lattice distortion and homopolar V-V bonding.

ACKNOWLEDGMENTS

The authors gratefully acknowledge support from the U.S. Army Research Laboratory and the U.S. Army Research Office under Contract No. W911NF-15-1-0448.

[1] F. J. Morin, Phys. Rev. Lett. **3**, 34 (1959).
[2] J. B. Goodenough, J. Solid State Chem. **3**, 490 (1971).
[3] A. Cavalleri, T. Dekorsy, H. H. W. Chong, J. C. Kieffer, and R. W. Schoenlein, Phys. Rev. B **70**, 161102(R) (2004).
[4] M. Imada, A. Fujimori, and Y. Tokura, Rev. Mod. Phys. **70**, 1039 (1998).
[5] E. Dagotto, Science **309**, 257 (2005).
[6] P. A. Lee, N. Nagaosa, and X.-G. Wen, Rev. Mod. Phys. **78**, 17 (2006).
[7] J. Sakai and M. Kurisu, Phys. Rev. B **78**, 033106 (2008).
[8] T. Kikuzuki and M. Lippmaa, Appl. Phys. Lett. **96**, 132107 (2010).

[9] X. Tan, T. Yao, R. Long, Z. Sun, Y. Feng, H. Cheng, X. Yuan, W. Zhang, Q. Liu, C. Wu, Y. Xie, and S. Weib, Sci. Rep. **2**, 466 (2012).

[10] A. Cavalleri, C. Tóth, C. W. Siders, J. A. Squier, F. Ráksi, P. Forget, and J. C. Kieffer, Phys. Rev. Lett. **87**, 237401 (2001).

[11] M. F. Becker, A. B. Buckman, R. M. Walser, T. Lepine, P. Georges, and A. Brun, Appl. Phys. Lett. **65**, 1507 (1994).

[12] M. M. Qazilbash, M. Brehm, B. Chae, P.-C. Ho, G. O. Andreev, B. Kim, S. Yun, A. V. Balatsky, M. B. Maple, F. Keilmann, H. Kim, and D. N. Basov, Science **318**, 1750 (2007).

[13] S. Lysenko, A. Rua, V. Vikhnin, J. Jimenez, F. Fernandez, and H. Liu, Appl. Surf. Sci. **252**, 5512 (2006).

[14] K. Appavoo, B. Wang, N. F. Brady, M. Seo, J. Nag, R. P. Prasankumar, D. J. Hilton, S. T. Pantelides, and R. F. Haglund, Nano Lett. **14**, 1127 (2014).

[15] A. C. Jones, S. Berweger, J. Wei, D. Cobden, and M. B. Raschke, Nano Lett. **10**, 1574 (2010).

[16] S. Wall, L. Foglia, D. Wegkamp, K. Appavoo, J. Nag, R. F. Haglund, J. Stähler, and M. Wolf, Phys. Rev. B **87**, 115126 (2013).

[17] H.-T. Kim, Y. W. Lee, B.-J. Kim, B.-G. Chae, S. J. Yun, K.-Y. Kang, K.-J. Han, K.-J. Yee, and Y.-S. Lim, Phys. Rev. Lett. **97**, 266401 (2006).

[18] C. Kübler, H. Ehrke, R. Huber, R. Lopez, A. Halabica, R. F. Haglund, and A. Leitenstorfer, Phys. Rev. Lett. **99**, 116401 (2007).

[19] D. J. Hilton, R. P. Prasankumar, S. Fourmaux, A. Cavalleri, D. Brassard, M. A. El Khakani, J. C. Kieffer, A. J. Taylor, and R. D. Averitt, Phys. Rev. Lett. **99**, 226401 (2007).

[20] X. Xue, M. Jiang, G. Li, X. Lin, G. Ma, and P. Jin, J. Appl. Phys. **114**, 193506 (2013).

[21] M. Nakajima, N. Takubo, Z. Hiroi, Y. Ueda, and T. Suemoto, Appl. Phys. Lett. **92**, 011907 (2008).

[22] D. B. McWhan, M. Marezio, J. P. Remeika, and P. D. Dernier, Phys. Rev. B **10**, 490 (1974).

[23] M. Hada, K. Okimura, and J. Matsuo, Phys. Rev. B **82**, 153401 (2010).

[24] M. W. Haverkort, Z. Hu, A. Tanaka, W. Reichelt, S. V. Streltsov, M. A. Korotin, V. I. Anisimov, H. H. Hsieh, H. J. Lin, C. T. Chen, D. I. Khomskii, and L. H. Tjeng, Phys. Rev. Lett. **95**, 196404 (2005).

[25] A. Cavalleri, M. Rini, H. H. W. Chong, S. Fourmaux, T. E. Glover, P. A. Heimann, J. C. Kieffer, and R. W. Schoenlein, Phys. Rev. Lett. **95**, 067405 (2005).

[26] A. Cavalleri, H. H. W. Chong, S. Fourmaux, T. E. Glover, P. A. Heimann, J. C. Kieffer, B. S. Mun, H. A. Padmore, and R. W. Schoenlein, Phys. Rev. B **69**, 153106 (2004).

[27] B.-J. Kim, Y. W. Lee, S. Choi, J.-W. Lim, S. J. Yun, H.-T. Kim, T.-J. Shin, and H.-S. Yun, Phys. Rev. B **77**, 235401 (2008).

[28] P. Baum, D.-S. Yang, and A. H. Zewail, Science **318**, 788 (2007).

[29] V. R. Morrison, R. P. Chatelain, K. L. Tiwari, A. Hendaoui, A. Bruhács, M. Chaker, and B. J. Siwick, Science **346**, 445 (2014).

[30] V. A. Lobastov, J. Weissenrieder, J. Tang, and A. H. Zewail, Nano Lett. **7**, 2552 (2007).

[31] H. T. Kim, B. G. Chae, D. H. Youn, S. L. Maeng, G. Kim, K. Y. Kang, and Y. S. Lim, New J. Phys. **6**, 52 (2004).

[32] J. M. Booth and P. S. Casey, Phys. Rev. Lett. **103**, 086402 (2009).

[33] S. Kim, K. Kim, C.-J. Kang, and B. I. Min, Phys. Rev. B **87**, 195106 (2013).

[34] T. Yao, X. Zhang, Z. Sun, S. Liu, Y. Huang, Y. Xie, C. Wu, X. Yuan, W. Zhang, Z. Wu *et al.*, Phys. Rev. Lett. **105**, 226405 (2010).

[35] T. L. Cocker, L. V. Titova, S. Fourmaux, G. Holloway, H. C. Bandulet, D. Brassard, J. C. Kieffer, M. A. El Khakani, and F. A. Hegmann, Phys. Rev. B **85**, 155120 (2012).

[36] See Supplemental Material at http://link.aps.org/supplemental/10.1103/PhysRevB.95.235157 for additional figures and accompanying text, which includes Refs. [74–84].

[37] J. C. Stover, *Optical Scattering: Measurements and Analysis* (SPIE Optical Engineering Press, Bellingham, Washington, 1995).

[38] M. Zerrad, M. Lequime, and C. Amra, Appl. Opt. **53**, A297 (2014).

[39] T. Herffurth, S. Schröder, M. Trost, A. Duparré, and A. Tünnermann, Appl. Opt. **52**, 3279 (2013).

[40] J. E. Harvey, S. Schröder, N. Choi, and A. Duparré, Opt. Eng. **51**, 013402 (2012).

[41] J. Sorrentini, M. Zerrad, and C. Amra, Opt. Lett. **34**, 2429 (2009).

[42] See Supplemental Material at http://link.aps.org/supplemental/10.1103/PhysRevB.95.235157 for relative change of UDC indicatrix movie of VO_2 film on A-cut Al_2O_3.

[43] C. F. Bohren and D. P. Huffman, *Absorption and Scattering of Light by Small Particles* (John Wiley & Sons, New York, 1983).

[44] H. W. Verleur, A. S. Barker, and C. N. Berglund, Phys. Rev. **172**, 788 (1968).

[45] S. Lysenko, F. Fernández, A. Rúa, and H. Liu, J. Appl. Phys. **114**, 153514 (2013).

[46] S. Lysenko, F. Fernández, A. Rúa, N. Sepúlveda, and J. Aparicio, Appl. Opt. **54**, 2141 (2015).

[47] Z. Tao, F. Zhou, T.-R. T. Han, D. Torres, T. Wang, N. Sepulveda, K. Chang, M. Young, R. R. Lunt, and C.-Y. Ruan, Sci. Rep. **6**, 38514 (2016).

[48] R. Yusupov, T. Mertelj, V. V. Kabanov, S. Brazovskii, P. Kusar, J.-h. Chu, I. R. Fisher, and D. Mihailovic, Nat. Phys. **6**, 681 (2010).

[49] T. Huber, S. O. Mariager, A. Ferrer, H. Schäfer, J. A. Johnson, S. Grübel, A. Lübcke, L. Huber, T. Kubacka, C. Dornes, C. Laulhe, S. Ravy, G. Ingold, P. Beaud, J. Demsar, and S. L. Johnson, Phys. Rev. Lett. **113**, 026401 (2014).

[50] A. P. Levanyuk and D. G. Sannikov, Sov. Phys. Usp. **17**, 199 (1974).

[51] S. Wall, D. Wegkamp, L. Foglia, K. Appavoo, J. Nag, R. F. Haglund, J. Stähler, and M. Wolf, Nat. Commun. **3**, 721 (2012).

[52] A. Pashkin, C. Kübler, H. Ehrke, R. Lopez, A. Halabica, R. F. Haglund, Jr., R. Huber, and A. Leitenstorfer, Phys. Rev. B **83**, 195120 (2011).

[53] B. A. Strukov and A. P. Levanyuk, *Ferroelectric Phenomena in Crystals: Physical Foundations* (Springer-Verlag, Berlin, Heidelberg, 1998).

[54] C. Ott, M. F. Jager, C. J. Kaplan, R. E. Marvel, R. F. Haglund, D. M. Neumark, and S. R. Leone, *International Conference on Ultrafast Phenomena*, UTu4A 48 (2016).

[55] D. Wegkamp, M. Herzog, L. Xian, M. Gatti, P. Cudazzo, C. L. McGahan, R. E. Marvel, R. F. Haglund, A. Rubio, M. Wolf, and J. Stähler, Phys. Rev. Lett. **113**, 216401 (2014).

[56] Z. Tao, T.-R. T. Han, S. D. Mahanti, P. M. Duxbury, F. Yuan, C.-Y. Ruan, K. Wang, and J. Wu, Phys. Rev. Lett. **109**, 166406 (2012).
[57] M. Liu, M. Wagner, E. Abreu, S. Kittiwatanakul, A. McLeod, Z. Fei, M. Goldflam, S. Dai, M. Fogler, J. Lu *et al.*, Phys. Rev. Lett. **111**, 096602 (2013).
[58] J. Laverock, S. Kittiwatanakul, A. A. Zakharov, Y. R. Niu, B. Chen, S. A. Wolf, J. W. Lu, and K. E. Smith, Phys. Rev. Lett. **113**, 216402 (2014).
[59] B. Hong, K. Hu, Z. Tao, J. Zhao, N. Pan, X. Wang, M. Lu, Y. Yang, Z. Luo, and C. Gao, Phys. Rev. B **95**, 075433 (2017).
[60] W.-P. Hsieh, M. Trigo, D. A. Reis, G. Andrea Artioli, L. Malavasi, and W. L. Mao, Appl. Phys. Lett. **104**, 021917 (2014).
[61] L. Bai, Q. Li, S. A. Corr, Y. Meng, C. Park, S. V. Sinogeikin, C. Ko, J. Wu, and G. Shen, Phys. Rev. B **91**, 104110 (2015).
[62] H. He, H. Gao, W. Wu, S. Cao, J. Hong, D. Yu, G. Deng, Y. Gao, P. Zhang, H. Luo *et al.*, Phys. Rev. B **94**, 205127 (2016).
[63] E. Arcangeletti, L. Baldassarre, D. Di Castro, S. Lupi, L. Malavasi, C. Marini, A. Perucchi, and P. Postorino, Phys. Rev. Lett. **98**, 196406 (2007).
[64] J. Wu, Q. Gu, B. S. Guiton, N. P. de Leon, L. Ouyang, and H. Park, Nano Lett. **6**, 2313 (2006).
[65] J. Cao, E. Ertekin, V. Srinivasan, W. Fan, S. Huang, H. Zheng, J. Yim, D. Khanal, D. Ogletree, J. Grossman *et al.*, Nat. Nanotechnol. **4**, 732 (2009).
[66] B. Hu, Y. Ding, W. Chen, D. Kulkarni, Y. Shen, V. V. Tsukruk, and Z. L. Wang, Adv. Mater. **22**, 5134 (2010).
[67] A. Tselev, I. Luk'yanchuk, I. Ivanov, J. Budai, J. Tischler, E. Strelcov, A. Kolmakov, and S. Kalinin, Nano Lett. **10**, 4409 (2010).
[68] B. Hu, Y. Zhang, W. Chen, C. Xu, and Z. L. Wang, Adv. Mater. **23**, 3536 (2011).
[69] J. Laverock, A. Preston, D. Newby, Jr., K. Smith, S. Sallis, L. Piper, S. Kittiwatanakul, J. Lu, S. Wolf, M. Leandersson *et al.*, Phys. Rev. B **86**, 195124 (2012).
[70] N. B. Aetukuri, A. X. Gray, M. Drouard, M. Cossale, L. Gao, A. H. Reid, R. Kukreja, H. Ohldag, C. A. Jenkins, E. Arenholz *et al.*, Nat. Phys. **9**, 661 (2013).
[71] S. Kumar, J. P. Strachan, M. D. Pickett, A. Bratkovsky, Y. Nishi, and R. S. Williams, Adv. Mater. **26**, 7505 (2014).
[72] L. Fan, S. Chen, Z. Luo, Q. Liu, Y. Wu, L. Song, D. Ji, P. Wang, W. Chu, C. Gao *et al.*, Nano Lett. **14**, 4036 (2014).
[73] S. Kittiwatanakul, S. A. Wolf, and J. Lu, Appl. Phys. Lett. **105**, 073112 (2014).
[74] K. H. Bennemann, J. Phys.: Condens. Matter **23**, 073202 (2011).
[75] V. S. Vikhnin, S. Lysenko, A. Rua, F. Fernandez, and H. Liu, Solid State Commun. **137**, 615 (2006).
[76] Z. P. Wu, A. Miyashita, I. Nashiyama, and H. Naramoto, Philos. Mag. Lett. **79**, 813 (1999).
[77] M. S. Laad, L. Craco, and E. Müller-Hartmann, Phys. Rev. B **73**, 195120 (2006).
[78] K. Chenoweth, A. C. T. van Duin, and W. A. Goddard, J. Phys. Chem. A **112**, 1040 (2008).
[79] M. van Veenendaal, Phys. Rev. B **87**, 235118 (2013).
[80] K. Hefferan and J. O'Brien, *Earth Materials* (Wiley-Blackwell, 2010).
[81] M. Gatti, F. Bruneval, V. Olevano, and L. Reining, Phys. Rev. Lett. **99**, 266402 (2007).
[82] B. T. O'Callahan, A. C. Jones, J. Hyung Park, D. H. Cobden, J. M. Atkin, and M. B. Raschke, Nat. Commun. **6**, 6849 (2015).
[83] Atomistix ToolKit version 2014.2 (QuantumWise A/S, 2014).
[84] J. M. Longo and P. Kierkegaard, Acta Chem. Scand. **24**, 420 (1970).

Supplementary Information

Ultrafast diffraction conoscopy of VO_2 structural phase transition: evidence of two lattice distortions

Nardeep Kumar, Armando Rúa, Félix E. Fernández, Sergiy Lysenko

Department of Physics, University of Puerto Rico, Mayaguez, Puerto Rico 00681, USA

Table of contents:

1. Surface topography of VO_2 thin film samples

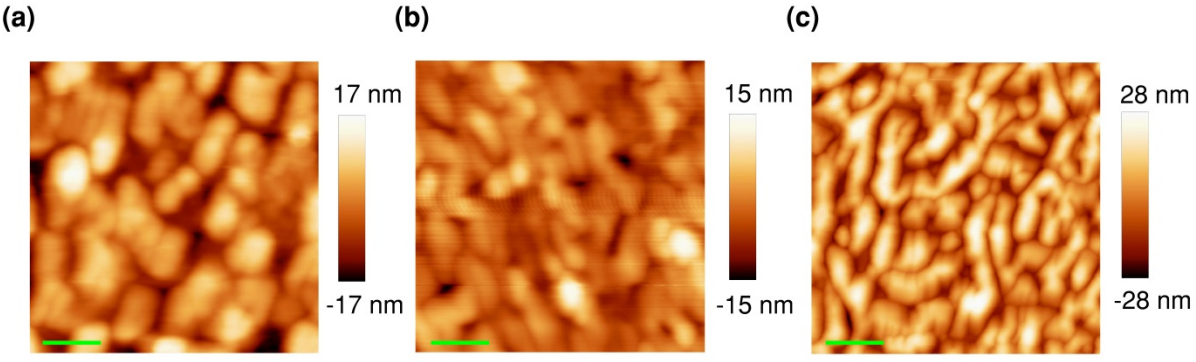

Supplementary Figure 1: Surface topography of VO_2 thin film samples observed by Atomic Force Microscope (AFM). (a) 40 nm VO_2 on A-cut Al_2O_3. (b) 80 nm VO_2 on A-cut Al_2O_3. (c) 80 nm VO_2 on M-cut Al_2O_3. The average grain size and root mean square roughness values in each case are, respectively: ~125 nm and 5.9 nm rms, ~100 nm and 3.1 nm rms, and ~90 nm and 9.4 nm rms. Scale bars: 200 nm.

2. Structural features of VO_2 thin film samples

X-ray diffraction scans of the samples were obtained with a Bruker D8 Discover diffractometer equipped with a copper target X-ray tube and a Göbel mirror. Supplementary Figure 2(a) shows the XRD patterns (θ-2θ scans) for the 40 nm (black curve) and 80 nm (blue curve) VO_2 films deposited on A-cut Al_2O_3, using a logarithmic scale for the number of counts. The substrate causes the very strong peak at 37.70°, which corresponds to the $(110)_{Al2O3}$ reflection, as well as ghost peaks due to Cu K_β radiation left over by the Göbel mirror and a small contribution from tungsten L_α radiation caused by this element being deposited from the filament onto the copper target of the X-ray tube as it ages. These extra peaks are indicated in the Supplementary Figure 2(a) and can be disregarded.

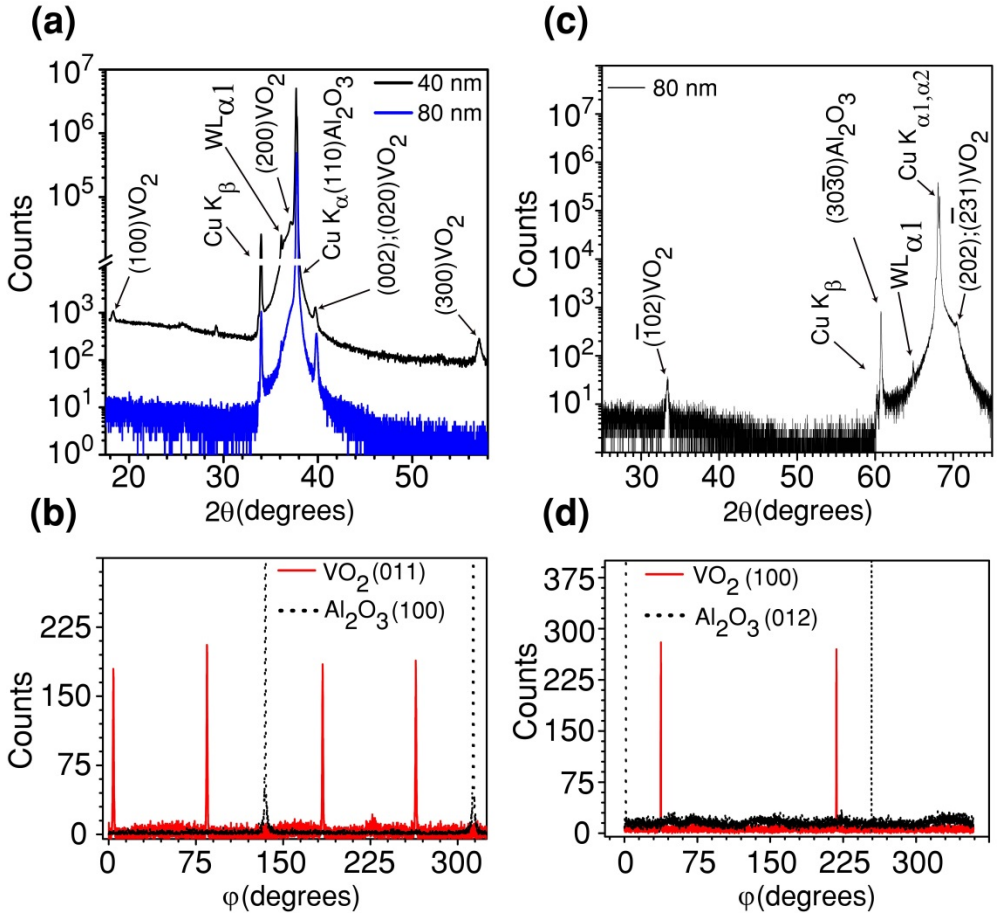

Supplementary Figure 2: The XRD patterns of the VO_2 thin film samples. (a) XRD patterns of 40 nm (black curve) and 80 nm (blue curve) VO_2 films on A-cut Al_2O_3 with θ-2θ scans. (b) X-ray diffraction intensity versus azimuthal orientation of the sample for 40 nm thick VO_2 films on A-cut Al_2O_3 substrate. (c) XRD patterns of 80 nm thick VO_2 film grown on M-cut Al_2O_3 substrates. (d) X-ray diffraction intensity versus azimuthal orientation of the sample for 80 nm thick VO_2 films on M-cut Al_2O_3 substrate.

For the thicker (80 nm) film [lower curve in Supplementary Figure 2(a)] the only peak not due to the sapphire substrate is located near 39.72° and can be directly assigned to the M_1 (monoclinic) VO_2 phase (020) reflection, although the (002) reflection is very close for strain-

free crystals or powders, according to Powder Diffraction File JCPDS #82-0661, and strain in the films could easily cause a shift equal or even larger than the difference (~0.07°) for unstrained positions. It is also possible that both reflections are present, but the respective peaks were not resolved in our scans. The second order reflection, attributable as (040), was also clearly observed by $2\theta = 85.73°$ [not shown in Supplementary Figure 2(a)], although again it is possible that the (004) reflection is present but unresolved. None of the other possible reflections from VO_2 (M_1), some of which are much stronger lines, were observed. Hence the 80 nm film shows excellent out-of-plane orientation over the sapphire substrate, likely with $(010)_m$ planes parallel to its surface (and therefore the b_m axis normal to the surface), and possibly with a fraction of crystallites oriented with their $(001)_m$ planes parallel to the substrate surface.

To study in-plane orientation of the film crystallites, several azimuthal scans (φ-scans) on the sample were performed. Each of these scans is performed at a fixed inclination angle χ (polar angle in a pole representation) between the sample surface plane and a different selected crystal plane with strong reflections. The inclination angle is calculated and set in each case from the known crystal structure of the material. The detector is fixed at the 2θ angle for the expected reflection. For the thicker (80 nm) film on A-cut sapphire, the results evidenced very sharp in-plane orientation, but it appears that both possibilities for the out-of-plane orientations mentioned above coexist. In the first case (i. e. $(010)_m$ planes parallel to the substrate surface), which is likely dominant, the film a_m axis is along the substrate surface and perpendicular to its c axis. In the second case (i. e. $(001)_m$ planes parallel to the substrate surface) the film b_m axis is along the substrate surface and parallel to its c axis. Thus, the film appears to consist of two distinct groups of crystallites, each of them highly textured with respect to the substrate structure.

The upper curve in Supplementary Figure 2(a) is the θ-2θ scan obtained for the thinner (40 nm) film deposited on A-cut sapphire. The major difference in this XRD pattern, when compared with the one for the 80 nm film, is the appearance of $(100)_m$, $(200)_m$, and $(300)_m$ diffraction peaks for monoclinic VO_2. Moreover, the relative intensities for this film of the $(020)_m$ peak (shown in the figure) and $(040)_m$ peak (not shown in the figure) are much weaker. Hence, it seems that for the early stages of growth, at least for the conditions employed in the present case, the $(100)_m$ orientation (or rather the equivalent surface for the tetragonal VO_2 phase, since that is the stable structure at the deposition temperature) competes with the other orientations observed, particularly $(010)_m$, but is disfavoured once the film is thicker. This fact suggests that there is strong misfit strain in the thinner film, which is related to the formation of substantially different, energetically favourable domain patterns. Thus, in addition to crystal domains as described for the thicker sample, the 40 nm sample includes domains $(100)_m||(110)_{Al2O3}$, so that b_m and c_m axes are parallel to the substrate surface. From the relative intensities of the reflections observed, it appears that this latter case may be favoured during initial stages of growth.

Supplementary Figure 2(b) shows azimuthal φ-scans for the sample with the 40 nm film. The scan for the substrate (black dot curve) was performed by setting $\chi = 30°$, which is the angle between the sapphire $(110)_{Al2O3}$ and $(100)_{Al2O3}$ planes (the latter would correspond to an M-cut). As expected from the symmetry, two peaks separated by 180° are observed. Thus, the sapphire c direction corresponds to angles exactly in-between these peaks. The inclination angle was then changed to observe the strongest monoclinic VO_2 reflection at $\chi = 67.6°$, which is $(011)_m$, assuming that the film $(100)_m$ planes are parallel to the sample surface. The result is the red curve in Supplementary Figure 2(b). In this case, four diffraction peaks are obtained, separated by 80.5° and 99.5° as expected for the VO_2 crystal. This information allows us to define the

actual orientation of c_m and b_m crystallographic directions on the sample surface for the $(100)_m||(110)_{Al2O3}$ crystallites. In this case, the film c_m axis is parallel to the sapphire c axis. From symmetry, there are two orientations (turned 180° around the surface normal) of the VO_2 crystal which satisfy these conditions, and the fact that the φ-scan peaks obtained have equal intensities show that the two occurrences, as could be expected, are equally distributed.

Similarly, results of the θ-2θ scan for the ~80 nm thick sample grown on m-plane sapphire are shown in Supplementary Figure 2(c). Film peaks are attributed to M_1-phase VO_2 reflections $(\bar{1}02)$, at 33.39°, and (202)/$(\bar{2}31)$, both at 70.43°. The values for the 2θ angles obtained agree very well with those given in JCPDS file # 82-0661 and are nearly the same as for similar (but thicker) samples grown under nominally the same conditions. Since these are relatively weak reflections for M_1-phase VO_2 and none of the much stronger reflections was observed, the results demonstrate preferential growth orientations corresponding to the planes indicated. The strong in-plane orientation of the film was also observed, through φ-scans. In Supplementary Figure 2(d), for example, the φ scan for the substrate is obtained by using the sapphire [100] direction as pole and seeking the equivalent (012) and $(1\bar{1}2)$ reflections (inclination at $\chi = 65.03°$). These are found with an azimuthal separation $\Delta\varphi = 107.25°$, which is almost exactly the value which can be calculated from the sapphire structure. Then the normal to the film (101) plane was used as a pole, and the (100) reflection (inclination at $\chi = 29.74°$) was sought. As seen from the figure, two reflections were found, with equal intensities, separated by $\Delta\varphi = 180°$, and with azimuthal separation of +36° and -36° from each of the substrate peaks. This result indicates that the crystallites with (101) planes parallel to the substrate surface are formed by twins flipped by 180° around the surface normal. It is expected that misfit between VO_2 and the sapphire m-plane can produce strong strain, particularly for very thin films. In fact, it has been stated before that VO_2 films grown by PLD on m-plane sapphire can exhibit the M_2 phase or M_1 phase, or both, depending on growth conditions, and that lower misfit strain can favor M_2 formation at the early stages of growth[1]. While we did not observe in our samples any reflections attributable to the M_2 phase, it can be expected that crystallites are strongly strained.

3. Uniaxial and biaxial indicatrix and conoscopy patterns

Uniaxial crystal is defined by a single optical axis and two refractive indices n_o and n_e. Optical indicatrix of uniaxial crystal is a spheroid with two equal semi-axes n_o Supplementary Figure 3(a)]. On the other hand, a biaxial crystal is defined by two optical axes and three different refractive indices n_1, n_2 and n_3. Its optical indicatrix is an ellipsoid as shown in Supplementary Figure 3(c). In regular conoscopy, the conoscopy image is a combination of different patterns such as isochromes, isogyres and melatopes[2]. There is a very distinct difference between conoscopy patterns for uniaxial and biaxial crystals when viewed in cross- polarized light. In the case of uniaxial crystals, a distinct conoscopy image contains a dark cross of extinction called isogyre [Supplementary Figure 3(b)]. A point at the centre of the isogyres, which defines the projection of the optic axis, is called a melatope. The major pattern in the case of biaxial crystals is made up of two melatopes [Supplementary Figure 3(d)] due to the presence of two optic axes. The angle between the two optic axes is called angle 2V. This angle is proportional to the separation between the melatopes. Usually, the biaxial crystal has two well-separated melatopes, while for uniaxial crystal the separation between the melatopes is zero. Such distinctive patterns highly depend on crystal symmetry and, hence, are useful to distinguish between different types of crystals.

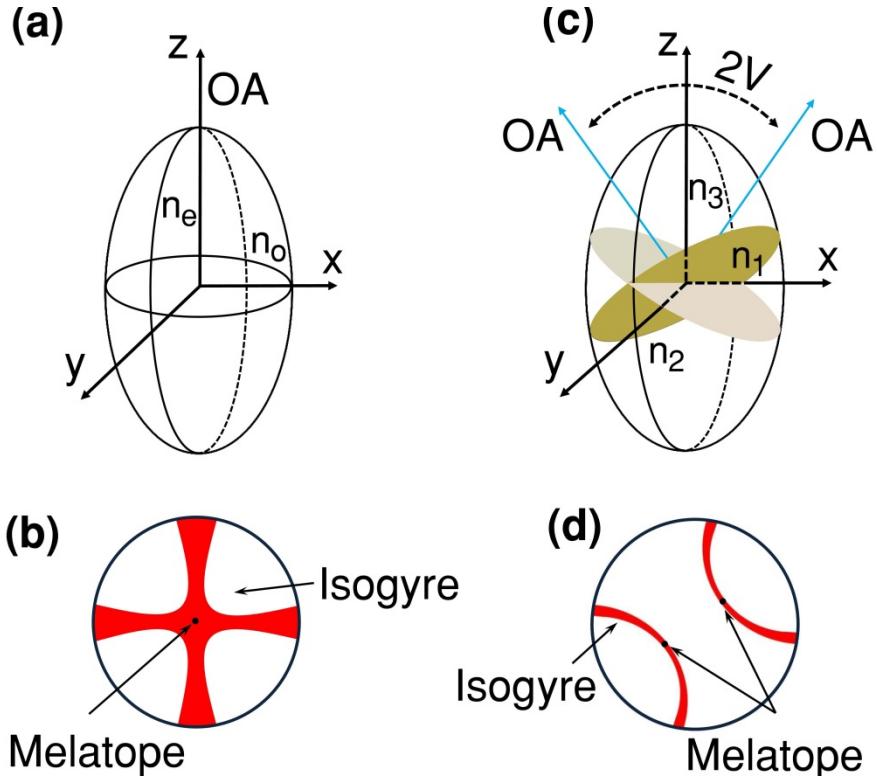

Supplementary Figure 3: Uniaxial and Biaxial indicatrix and conoscopy patterns. (a) Uniaxial indicatrix with two extinction directions represented by n_o and n_e rays. (b) Uniaxial conoscopy pattern, viewed along the optic axis (OA). Two red bars forming a cross are isogyres. The black dot at the centre where the optic axis emerges represents a melatope point. (c) Biaxial indicatrix with three principal indices of refraction n_1, n_2, and n_3. Two optic axes (OA) separated by 2V angle are shown by two blue arrow perpendicular to two circular cross-sections (brass and bone colors) of biaxial indicatrix. (d) Biaxial conoscopy pattern, viewed along one of its two optic axes. The points of maximum curvature for the isogyres (red color) are represented by two melatopes (black dots).

4. Ultrafast conoscopy of VO_2 on glass substrate

To compare the ultrafast diffraction conoscopy (UDC) dynamics for epitaxial and non-epitaxial films, additionally, we recorded UDC indicatrices for the 100-nm-thick VO_2 film deposited on glass substrate. This film is non-epitaxial with randomly oriented microcrystallites. As a result, the optical properties of this film are highly isotropic. The transient change ΔBSDF(*t*)/BSDF(0) of UDC patterns is shown in Supplementary Figure 4: the evolution of hemispherical differential indicatrix [Supplementary Fig. 4(a)] and the time-dependent cross-sections of indicatrices at φ=225° [Supplementary Fig. 4(b, c)]. As compared to epitaxial VO_2 films on Al_2O_3 substrate (Figs. 2, 3, and 7 of the main text), the differential UDC signal from VO_2/SiO_2 sample shows only a continuous decrease without any signature of the intermediate transient state. The optical response related solely to the structural dynamics of VO_2 cannot be detected in UDC experiments for optically isotropic samples. However, for highly-oriented epitaxial films, the UDC method provides a reliable monitoring of structural relaxation.

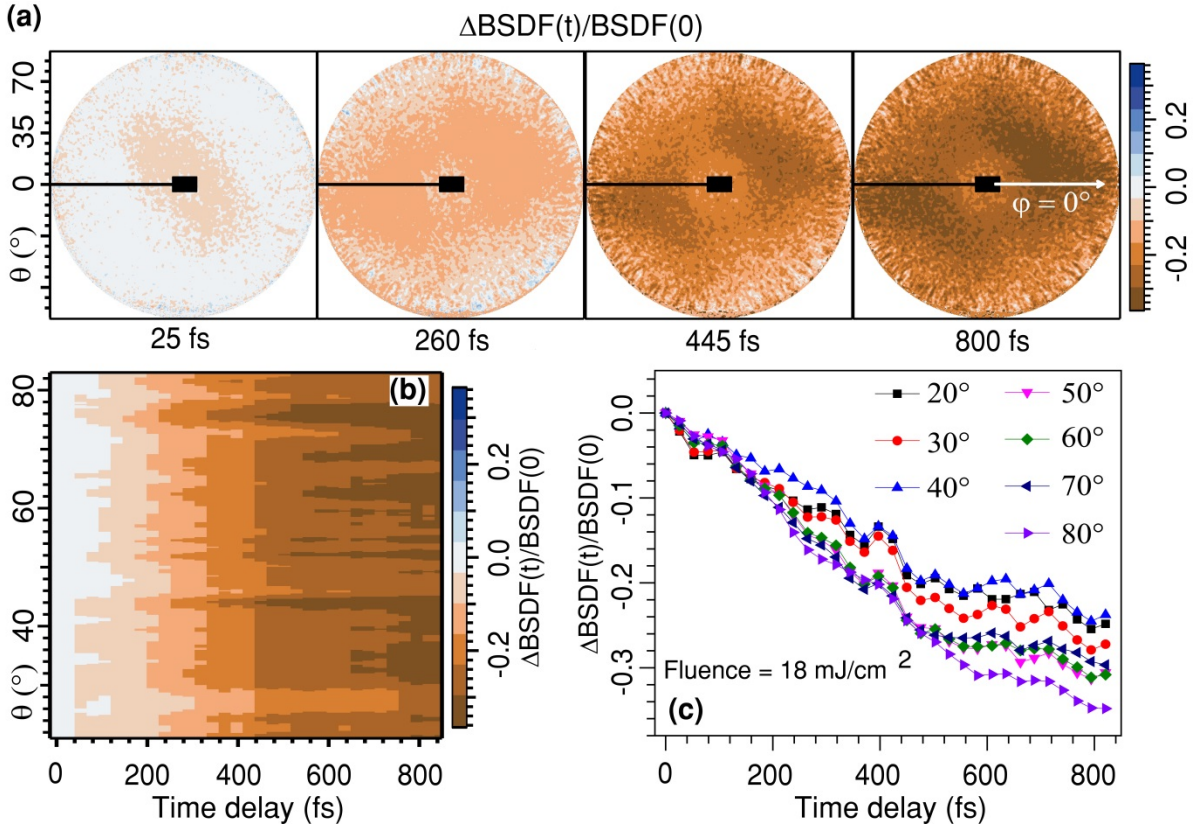

Supplementary Figure 4: The light scattering from 100-nm-thick VO_2 film on SiO_2. (a) Relative change ΔBSDF(t)/BSDF(0) of the UDC indicatrix. (b) Evolution of ΔBSDF(t)/BSDF(0) signal at φ=225° cross-section. (c) The cross-sections of the data mapped in (b) for various angles.

5. Coherent phonon dynamics in VO_2

Photoexcitation of VO_2 with energy near the VO_2 PT threshold (2-6 mJ/cm^2) activates coherent phonon mode near 6 THz frequency[3-7]. These oscillations were observed in our experiment when the system is switching into the intermediate transient state: they are visible in the supplementary movie for the transient differential conoscopy of 40-nm-thick VO_2/Al_2O_3 (A-cut) film. The movie shows some breathing like oscillations with a period of about 150 fs.

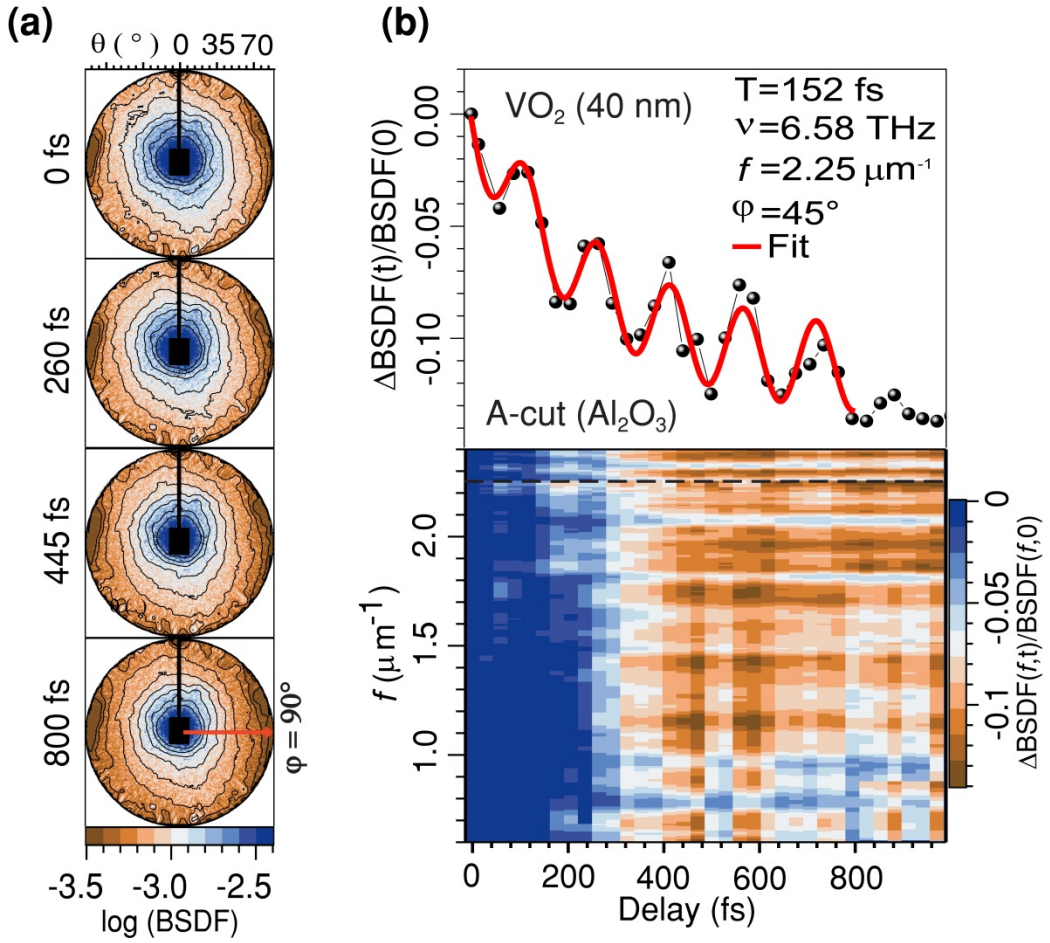

Supplementary Figure 5: Transient light scattering from the 40-nm-thick VO_2 film on A-cut Al_2O_3 without an analyzer at fluence F=6.8 mJ/cm^2. (a) Evolution of the BSDF indicatrix of hemispherical light scattering. (b) Lower panel: time-dependent cross-sections of the data mapped in (a) at φ =45° versus spatial frequency. Upper panel: the cross-section of the data mapped in the lower panel along the dashed line for the spatial frequency of f= 2.25μm^{-1}.

These coherent oscillations are observed during the entire relaxation process and are not related to the specific intermediate state. In our conoscopy results at a fluence of 14 mJ/cm^2, the near 6 THz coherent phonons are dominated by the intermediate phase and difficult to resolve. To better resolve these oscillations, the pump fluence was set near the PT threshold, at F=6.8 mJ/cm^2 without using an analyzer.

Supplementary Figure 5(a) shows the BSDF indicatrix of hemispherical light scattering from the 40-nm-thick VO_2 film on A-cut Al_2O_3 substrate. As expected, the scattering indicatrices show only a continuous decrease of the signal without any noticeable change of the pattern. Supplementary Figure 5(b), lower panel, shows time-dependent cross-sections of the scattering data mapped at azimuthal direction $\varphi = 45°$ versus spatial frequency. The transient response of the scattering signal with a time delay at different spatial frequencies shows a strong oscillatory behavior with a period of ~150 fs. To deduce the frequency of these oscillations we plot, in the upper panel, the cross-section of the data mapped in lower panel for the spatial frequency of f=2.25μm^{-1}. The transient scattering data was fitted using the following function:

$$\Delta BSDF(t)/BSDF(0) = A_0 + A_1 \sin[2\pi\nu(t-t_c)] + A_2 \exp(-t/t_1) \qquad (1)$$

where A_0, A_1 and A_2 are fitting amplitude constants, ν is the vibrational frequency, t_c is the phase shift constant and t_1 is the exponential time constant. Fitting of $\Delta BSDF(t)/BSDF(0)$ signal curve gives a period of 152 fs (ν=6.58 THz). This frequency matches well to the frequency of VO_2 modes studied previously[3-7]. The scattering map also shows a dependence of coherent lattice oscillations versus spatial frequency of the surface.

6. Displacement of VO_2 atoms on subpicosecond time scale: a computational study

The progress in the experimental and theoretical study of the PT in VO_2 evidence that the structural lattice transformation of VO_2 starts as a result of screening of electron correlations[8-11]. Moreover, it is likely that the photoinduced IMPT can be a Mott-type transition which occurs on the time scale of laser pulse interaction with the sample within several femtoseconds[8]. However, posterior structural transformation of VO_2 lattice from monoclinic to tetragonal (rutile) phase takes from ~80 fs to several hundred femtoseconds, depending on laser fluence, pulse duration and morphology of the sample. In this context, the molecular dynamics (MD) of VO_2 can be modelled by using computational methods which do not consider electron-electron correlations.

In order to perform semi-classical calculations of MD, we assumed that the role of ultrafast photoexcitation is only screening of electron-electron correlations, while all other physical characteristics of VO_2 lattice remain unchanged. This approximation is useful for quantitative estimation of atomic motion by modelling of VO_2 molecular dynamics within short timescale up to ~1 ps, when the process of energy transfer from electron to phonon subsystem can be neglected. In order to estimate a root-mean-square (*rms*) displacement of VO_2 atoms, we applied the ReaxFF reactive force field simulation of molecular dynamics[12], which is a part of the QuantumWise software package[13]. This semi-classical computation method does not consider electron-electron correlations but retains nearly the accuracy of quantum mechanical calculations. Also, it requires moderate computational resources and allows analysing large clusters.

Since electron correlations are not included into the ReaxFF method, it is suitable to model the situation of photoinduced screening of correlation effects in VO_2. In this case, the initial parameters of the VO_2 unit cell have to be chosen equal to experimentally measured ones, and MD is considered as an adiabatic process within the subpicosecond time scale, where the electron-phonon relaxation and energy exchange with a thermostat are neglected. The parameters of VO_2 unit cell were taken from experimentally obtained data in Ref. 14. The computation of VO_2 molecular dynamics was performed for a VO_2 (M_1) cluster of 20217 atoms. In order to

reduce the random component of atomic motion, the VO_2 temperature was set relatively low, as T=15 K.

Computational analysis of the VO_2 lattice within a broad range of temperatures from 1 K up to 315 K showed that the VO_2 unit cell is essentially unstable. Photoinduced screening of the electron correlations results in rearrangement of VO_2 atoms accompanied by kinetic energy release, similar to the exothermal chemical reaction. Since the ReaxFF method is semi-classical, it does not provide the exact trajectory of the VO_2 phase transition. Nevertheless, this method calculates *rms* displacement of VO_2 atoms which can be a very useful parameter for further analysis of VO_2 lattice transformation. Supplementary Figure 6 shows cumulative *rms* displacement of all VO_2 atoms versus time. Within 500 fs, the *rms* displacement is x_{rms} = 0.32 Å. We note, that this value is close to the effective displacement of VO_2 atoms of 0.26 Å, used by M. van Veenendaal in his theoretical work[15].

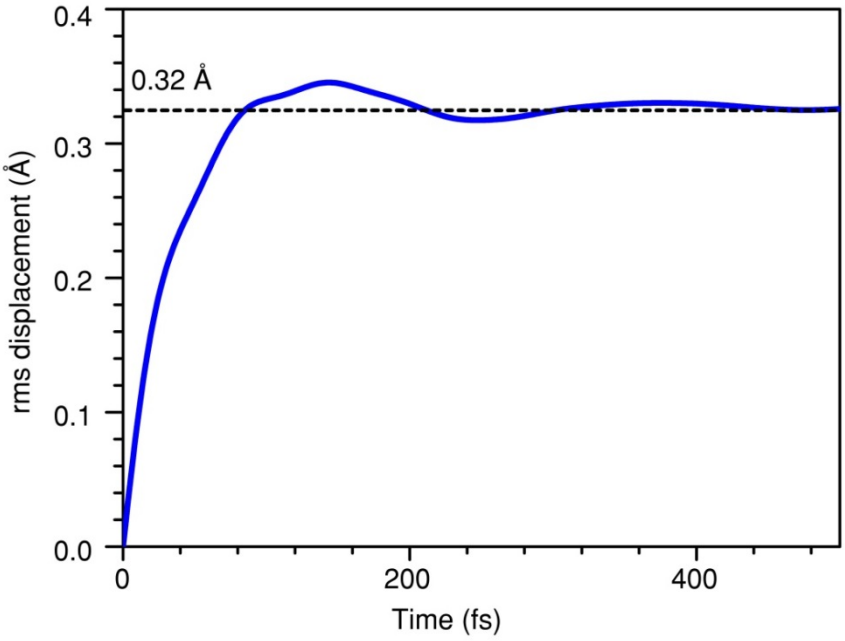

Supplementary Figure 6: Cumulative root-mean-square (rms) displacement of all VO_2 atoms. *rms* displacement of VO_2 atoms was estimated by applying ReaxFF reactive force field simulation of molecular dynamics from the QuantumWise software package.

7. Reconstruction of thermodynamic potential

In order to reconstruct the thermodynamic potential Φ of photoexcited VO_2, additional measurements of transient reflection and transmission were performed at different excitation levels. These measurements reveal two distinctive components of VO_2 relaxation dynamics. There is an instantaneous change of reflection coefficient within ~500 fs followed by posterior relaxation on a picosecond time scale (Supplementary Figure 7). This type of relaxation was observed previously by different authors, but while special attention was given in several works to this dynamic, it still needs rigorous study[5, 16-18]. The observed relaxation dynamics within 20 ps indicates that a certain group of VO_2 domains undergoes sub-picosecond PT, while the rest of the domains switch into metallic phase within several picoseconds. The slower relaxation of VO_2

lattice within picosecond time scale evidences the presence of a potential barrier ΔG between insulating and metallic phases, which alters the relaxation rate as[19].

$$\tau^{-1} = \tau_0^{-1} \exp(-\Delta G(F)/kT) \qquad (2)$$

here τ_0 is the minimal characteristic relaxation time and k is Boltzmann's constant. Above fluence, $F_0 = 30$ mJ/cm^2 the picosecond component of the PT was not detected. The time τ_0 was estimated, at F_0, to be 370 fs. Measurements of relaxation dynamics at different excitation levels allowed to derive $\Delta G \approx 0.05$ eV at laser pump fluence F = 10 mJ/cm^2, and to reconstruct the profile of one-dimensional Landau thermodynamic potential Φ as shown in Supplementary Figure 8(a). In order to model the observed two components of ultrafast IMPT, we present the obtained one-dimensional thermodynamic potential Φ for total lattice distortion (x) as an equivalent thermodynamic potential for two lattice distortions (x_1 and x_2) as shown in Supplementary Figure 8(b). In the model, for the sake of simplicity, we assume that the maximal ion displacement for each distortion is equal, where the sum of x_1 and x_2 distortions equals $x_{rms} = 0.32$ Å.

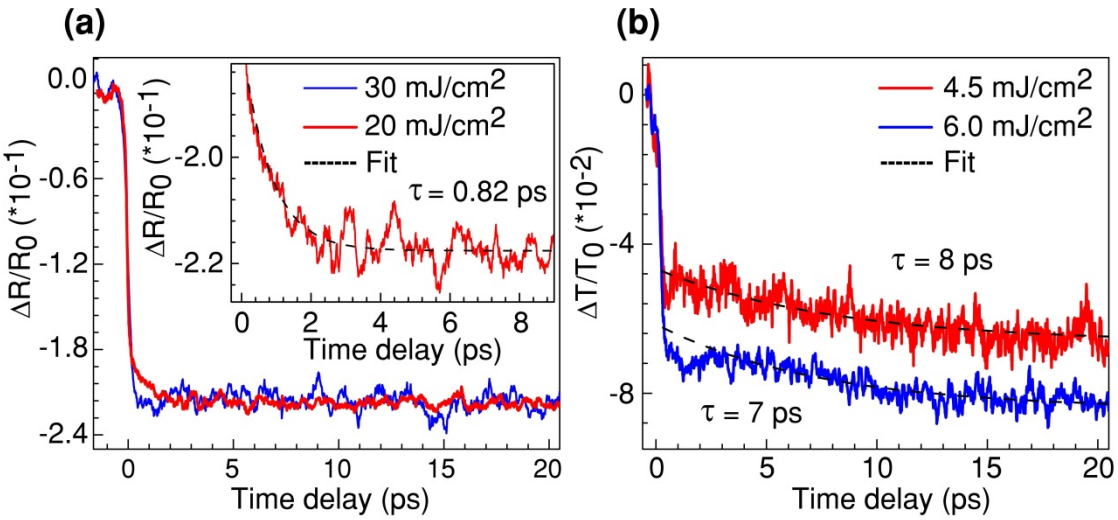

Supplementary Figure 7: Reflectivity/transmission responses of VO_2 films for 130 fs excitation pulses at 800 nm wavelength. (a) Transient differential reflection of VO_2 films at 20 mJ/cm^2 (blue curve) and 30 mJ/cm^2 (red curve) level of optical excitation. Both curves show two relaxations processes with fast and slow relaxations. The inset shows the differential reflection signal with single exponential fit for 20 mJ/cm^2 fluence. The fit gives the IMPT characteristic time on the order of 0.82 ps. (b) Differential transmission of VO_2 films obtained at 4.5 mJ/cm^2 (red curve) and 6.0 mJ/cm^2 (blue curve) laser fluence. Fits from the curves give longer IMPT characteristic time on the order of 8 ps (for the red curve) and 7 ps (for the blue curve).

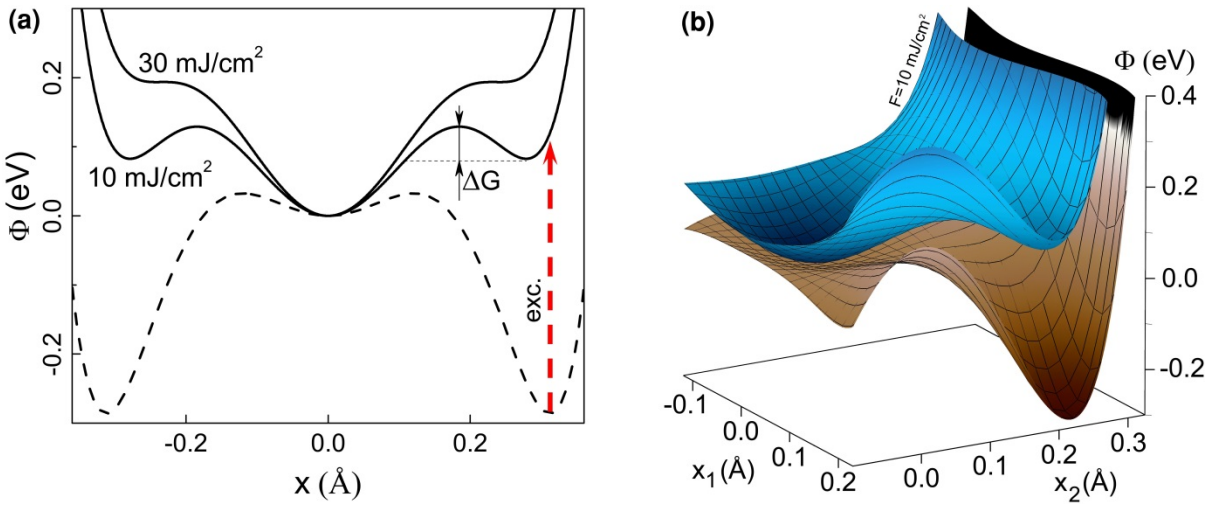

Supplementary Figure 8: Sketch of thermodynamic potential of VO_2 as a function of effective ion displacement. (a) A one-dimensional representation of thermodynamic potential as a function of cumulative lattice distortion (x) for the unperturbed (dashed line curve) and photoexcited (solid line curves) VO_2. (b) Thermodynamics potential as a function of two lattice distortions. The brown and blue energy surfaces represent unperturbed and photoexcited thermodynamic potential respectively.

References

[1] Z.P. Wu, A. Miyashita, I. Nashiyama, and H. Naramoto, Philos. Mag. Lett. **79**, 813 (1999).

[2] K. Hefferan and J. O'Brien, Earth Materials (Wiley-Blackwell, 2010).

[3] C. Kübler, H. Ehrke, R. Huber, R. Lopez, A. Halabica, R. F. Haglund, and A. Leitenstorfer, Phys. Rev. Lett. **99**, 116401 (2007).

[4] A. Pashkin, C. Kübler, H. Ehrke, R. Lopez, A. Halabica, R. F. Haglund, R. Huber, and A. Leitenstorfer, Phys. Rev.B **83**, 195120 (2011).

[5] S. Wall, L. Foglia, D. Wegkamp, K. Appavoo, J. Nag, R.F. Haglund, J. Stähler, and M. Wolf, Phys. Rev. B **87**, 115126 (2013).

[6] S. Wall, D. Wegkamp, L. Foglia, K. Appavoo, J. Nag, R. Haglund Jr, J. St□hler, and M. Wolf, Nat. Commun. **3**, 721 (2012).

[7] B. T. O'Callahan, A. C. Jones, J. Hyung Park, D. H. Cobden, J. M. Atkin, and M. B. Raschke, Nat. Commun. **6**, 6849 (2015).

[8] D. Wegkamp, M. Herzog, L. Xian, M. Gatti, P. Cudazzo, C.L. McGahan, R.E. Marvel, R.F. Haglund, A. Rubio, M. Wolf, and J. Stähler, Phys. Rev. Lett. **113**, 216401 (2014).

[9] V.S. Vikhnin, S. Lysenko, A. Rua, F. Fernandez, and H. Liu, Solid State Commun. **137**, 615 (2006).

[10] M.S. Laad, L. Craco, and E. Müller-Hartmann, Phys. Rev. B **73**, 195120 (2006).

[11] M. Gatti, F. Bruneval, V. Olevano, and L. Reining, Phys. Rev. Lett. **99**, 266402 (2007).

[12] K. Chenoweth, A.C.T. van Duin, and W.A. Goddard, J. Phys. Chem. A **112**, 1040 (2008).

[13] *Atomistix ToolKit* version 2014.2 (QuantumWise A/S, 2014).

[14] J. M. Longo and P. Kierkegaard, Acta Chem. Scand. **24**, 420 (1970).

[15] M. van Veenendaal, Phys. Rev. B **87**, 235118 (2013).

[16] P. Baum, D.-S. Yang, and A.H. Zewail, Science **318**, 788 (2007).

[17] T.L. Cocker, L. V. Titova, S. Fourmaux, G. Holloway, H.C. Bandulet, D. Brassard, J.C. Kieffer, M.A. El Khakani, and F.A. Hegmann, Phys. Rev. B **85**, 155120 (2012).

[18] K. Appavoo, B. Wang, N.F. Brady, M. Seo, J. Nag, R.P. Prasankumar, D.J. Hilton, S.T. Pantelides, and R.F. Haglund, Nano Lett. **14**, 1127 (2014).

[19] K.H. Bennemann, J. Phys.: Condens. Matter **23**, 073202 (2011).